AIAA JOURNAL
Vol. 45, No. 1, January 2007

Proportional Closed-Loop Feedback Control of Flow Separation

Jeremy T. Pinier,* Julie M. Ausseur,* Mark N. Glauser,† and Hiroshi Higuchi†
Syracuse University, Syracuse, New York 13244

DOI: 10.2514/1.23465

The aim of this experimental study is the implementation of a practical and efficient closed-loop feedback control of the turbulent flow over a NACA-4412 airfoil equipped with leading-edge zero-net-mass-flux actuators. By using prior computation of correlations between particle image velocimetry data and multiple surface pressure measurements, real-time instantaneous low-dimensional estimates of the velocity field over the wing are then computed from the unsteady surface pressure. From such estimates, a direct knowledge of the state of the flow above the airfoil is obtained (i.e., attached, incipient separation, or fully separated flow). We first show the effectiveness of the low-dimensional modeling approach in extracting and estimating the underlying large-scale structures in a turbulent flow, using the proper orthogonal decomposition and the modified linear/quadratic stochastic measurements. We then show how such an approach is used successfully in a simple, but practical, proportional feedback loop to delay the separation of the flow over the wing at high angles of attack. The benefits of closed-loop vs open-loop control are then discussed. These fundamental results validate the use of low-dimensional modeling techniques for further, more sophisticated, closed-loop feedback control algorithms.

Nomenclature

A_{ni}	=	linear coefficient of the modified linear stochastic measurement, mode n, ith pressure sensor
A'_{ni}, B'_{njk}	=	linear and quadratic coefficients of the modified quadratic stochastic measurement, mode n
$\mathrm{Act}_{\mathrm{input}}(t)$	=	unsteady actuation input
$a_n(t)$	=	proper orthogonal decomposition mode n expansion coefficient
$\tilde{a}_n(t)$	=	proper orthogonal decomposition/modified linear stochastic measurement mode n estimated expansion coefficient
$C(t, t')$	=	two-point temporal correlation tensor
C_μ	=	actuation momentum coefficient
c	=	chord length
f	=	frequency
f_o	=	actuation carrier frequency
f_s	=	pressure sampling frequency
f^+	=	reduced frequency, $f^+ = f \cdot c/U_\infty$
N	=	number of particle image velocimetry velocity vectors
N_m	=	number of modes
N_{tot}	=	total number of modes
n_c	=	number of velocity components
$p_i(t)$	=	ith unsteady pressure sensor
q	=	total number of pressure sensors
Re	=	Reynolds number based on chord length
$R_{ij}(\boldsymbol{x}, \boldsymbol{x}')$	=	ensemble averaged two-point spatial velocity correlation tensor
T	=	total number of particle image velocimetry snapshots
t	=	time stamp of particle image velocimetry snapshot
x, y, z	=	streamwise–wall normal–spanwise Cartesian coordinate system
U_∞	=	freestream velocity
u_i	=	ith component of velocity
α	=	angle of attack
α_s	=	uncontrolled stall angle of attack
$\lambda^{(n)}$	=	proper orthogonal decomposition mode n eigenvalue
ρ	=	density of air
$\phi_i^{(n)}(\boldsymbol{x})$	=	proper orthogonal decomposition mode n eigenfunction, ith component of velocity

Received 24 February 2006; revision received 4 August 2006; accepted for publication 20 August 2006.

*Student, Mechanical and Aerospace Engineering Department, 149 Link Hall. Student Member AIAA.

†Professor, Mechanical and Aerospace Engineering Department, 149 Link Hall. Associate Fellow AIAA.

I. Introduction

THE applications of flow control to high Reynolds number turbulent flows are numerous and can greatly improve the maneuverability and efficiency of vehicles exposed to such flows. Benefits in terms of drag reduction, by replacing traditional control surfaces with flow control devices, could be significant, all the more by using closed-loop control, as discussed further in this paper. Closed-loop flow control requires high-frequency sensing and actuating capabilities. With these frequencies often being higher on scaled-down laboratory models than on full-scale vehicles, the complexity of such experiments is even greater. As a result, real-time solutions to these problems become quite challenging. We, therefore, need low-dimensional tools that can reduce the complexity of the systems and extract only the features of the flow important for control (i.e., in this particular study, the large-scale events in the flow that are responsible for flow separation). The proper orthogonal decomposition (POD) [1] and the modified linear stochastic measurement (MLSM) [2,3] low-dimensional techniques are used here to capture and predict the most energetic structures in the flow from only wing surface pressure measurements. Note that the terminology has slightly changed from modified linear stochastic estimation (MLSE) to modified linear stochastic measurement, because estimation, in a control sense, is associated with estimating the dynamics of a system and not truly measuring the state of the system. Taylor and Glauser [3] showed, in the ActiveWing internal-flow facility at Clarkson University, that a five-mode proper orthogonal decomposition description of the flow was sufficiently accurate in describing the main features of the flow. Cohen et al. [4] have recently demonstrated POD-based feedback control for a very low Reynolds number external flow over a circular cylinder, indicating that such methods indeed apply to external flows. In their study, however, inflow velocity measurements are used to provide the POD coefficients and not surface measurements. The recent

application of POD/MLSM by Schmit and Glauser [5] to a micro air vehicle wake flow demonstrates the success of using these types of methods for external flows. They are able to obtain an accurate estimate of the velocity field in the wake, using only wing-mounted dynamic strain measurements. This paper summarizes our closed-loop control results since Glauser et al. [6], in which we showed our ability to get an accurate estimated measurement of the velocity field above the airfoil from surface pressure measurements only and later demonstrated POD/MLSM-based real-time proportional feedback control of a turbulent flow [7].

II. Experimental Setup

A. Facility and NACA-4412 Model Airfoil

The subsonic wind-tunnel facility at Syracuse University consists of a Göttingen-type, closed, recirculating design with the flow loop arranged in a horizontal configuration. The 0.61 m(w)× 0.61 m(h) × 2.44 m(l) test section is made of optical Plexiglas panels and is shown with the full experimental arrangement in Fig. 1. The flow speed in the test section is continuously variable from 5 to 67 m/s. A NACA-4412 airfoil with a 20.3-cm chord was selected for the experiments.

The test model shown in Figs. 1–3 is designed to meet several requirements. It is two-dimensional with a constant chord length and airfoil section geometry along the span. The model size was chosen to avoid significant blockage in the 0.61 × 0.61 m wind-tunnel test section. Actuator and pressure transducer inserts are configured in a modular fashion to enable rearrangement for further optimization and modifications. The wing span is 61 cm, thus covering the entire width of the test section, so that three-dimensional effects from wing tip vortices are negligible. Pressure and particle image velocimetry (PIV) measurements are taken at a midspan plane for which the flow is assumed to be two-dimensional in the mean sense. The experimental results presented here are performed at a freestream velocity of $U_\infty = 10$ m/s, corresponding to a Reynolds number based on chord length of 135,000. The uncontrolled stall angle of attack of the airfoil is $\alpha_s = 16$ deg at this Reynolds number.

Given the thickness distribution of the model, the most accessible location for actuator placement is in the first 10 to 30% of the chord length. This is a good choice because of the effectiveness of the actuation based on boundary-layer growth and flow separation location. The wing was machined from aluminum and divided along the span into three sections: a center section of 22.9 cm sandwiched between two 19.1-cm outer sections. These three main pieces are held in position with pins and fastened together by a threaded rod and no surface roughness is present at the joint. The angles of attack must be continuously variable, covering a range from attached to separated flow. Therefore, the wing is hinged on the sides of the wind tunnel, using a hollow tube that serves as an exit guide for the sensing and actuating wires. Both outer sections contain a 14.2-cm-long modular segment that houses four actuators each. The center section is composed of a similar segment that is 22.2-cm-long and houses six actuators in addition to a 12.7-cm-wide segment for the dynamic pressure transducers and static pressure ports. Overall, a total of 14 piezoelectric actuators are spread along the span of the wing.

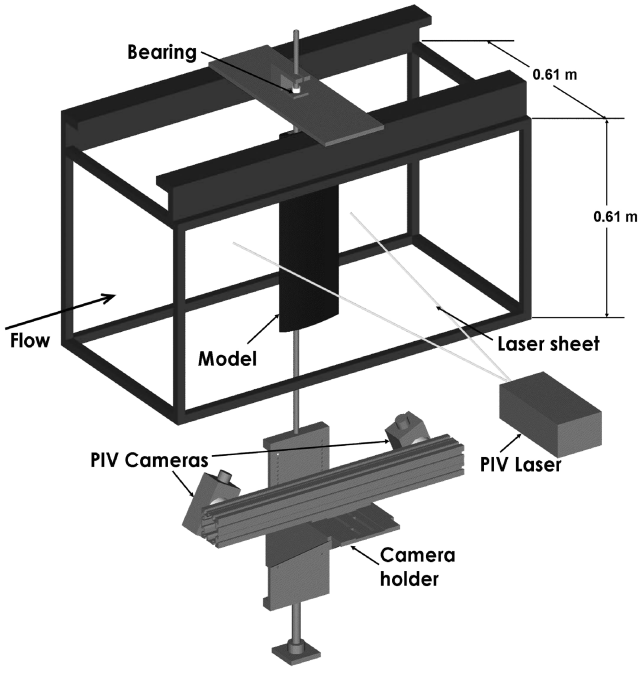

Fig. 1 Overall view of experimental setup located in the test section of the Syracuse University closed-loop low-speed wind tunnel.

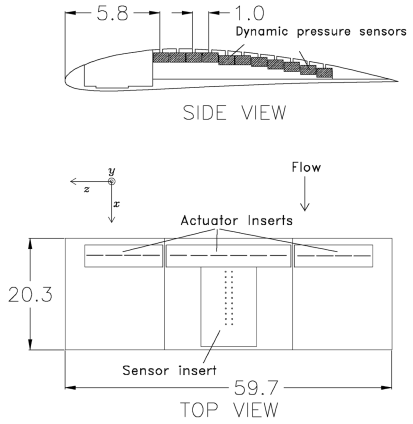

Fig. 2 Side and top view of NACA-4412 airfoil, cm.

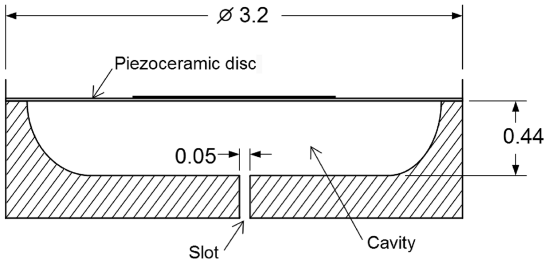

Fig. 3 Schematic of actuator/cavity system, cm.

B. Sensing and Actuating

To apply closed-loop control, both sensing and actuating devices are needed. In this setup, the actuators are placed upstream of the sensors, creating a feedback loop arrangement in which the pressure measurement significantly depends on the actuator output. The 11 unsteady pressure transducers are spaced evenly from $x/c = 0.29$ to $x/c = 0.78$, with a spacing between each transducer of $0.049x/c$. This leaves the remaining space for the actuator insert section (Fig. 2). The transducers are ICP pressure sensors from PCB Piezotronics, with a 2-psi (13.8 kPa) dynamic range, a 0.02-mpsi (0.138 Pa) resolution, and a bandwidth of 5–13 kHz. The sensors are miniature air turbulence sensors (9.5-mm diameter, 7.2-mm height) and were chosen because of their fast response characteristics and because of their small size.

The actuating system consists of 14 small oscillatory slot jets near the leading edge of the airfoil, produced by vibrating piezoceramic discs located in individual cavities under the surface of the airfoil. These synthetic jet actuators have been developed in part by the Amitay group at Rensselaer Polytechnic Institute. Detailed measurements of the synthetic jet flow and the design of these types of actuators can be found in Smith and Glezer [8] and Glezer and Amitay [9]. The cavity and actuator system, as shown in Fig. 3, has an exit slot of 0.5-mm wide and 30-mm long. The piezoelectric actuators are driven at the Helmholtz resonator frequency of the cavity so as to produce high-velocity oscillating jets at the exit of the slots. Each individual actuator/cavity system was calibrated using a hot wire anemometer to find each of the resonance frequencies and all

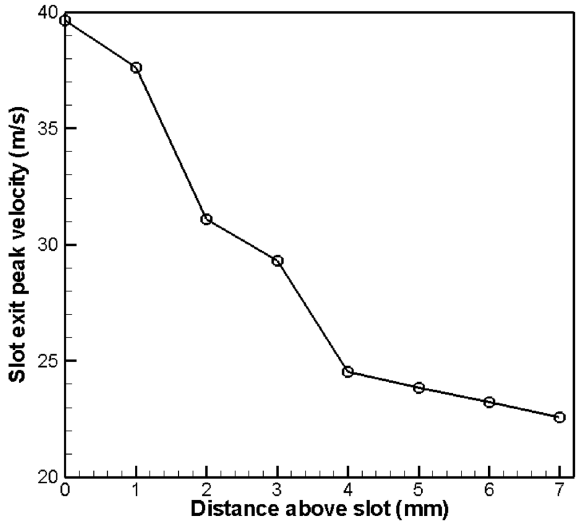

Fig. 4 Peak exit velocity from $y = 0$ to $y = 7$ mm above the actuator slot; 800-Hz actuation.

were found to be 750 ± 50 Hz. The maximum positive velocity measured from $y = 0$ to $y = 7$ mm above the actuating slots with no freestream flow is shown in Fig. 4, using an 800 Hz sine wave output. As can be observed, rather high oscillating velocities can be achieved at the exit, using these types of actuators. We can, from these values, estimate the amount of energy that is introduced in the boundary layer relative to the freestream flow, using the momentum coefficient, defined as [10]

$$C_\mu = \sum_i (\rho U_{\text{rms}}^2 A_i)/(\frac{1}{2}\rho U_\infty^2 A_w)$$

where A_i is the ith slot area, A_w is the plan view area of the wing, and U_{rms} is the root mean square (rms) exit velocity. Using these actuators, C_μ was calculated to be 0.02, with an uncertainty in this quantity evaluated at 20%.

C. Data Acquisition System

Both in-plane components of velocity, u and v, are measured using a Dantec Dynamics PIV System with two cameras side by side, to double the size of the measurement area in the x–y (streamwise–wall normal) plane above the airfoil. The PIV sampling frequency was 4 Hz, much slower than the time scales in the 10 m/s flow; therefore, all samples are statistically independent. The PIV system consists of two CCD cameras (1280×1024 pixels), a pair of pulsed New Wave Research 200 mJ Nd:YAG lasers, light sheet optics, and a postprocessing unit. An olive oil seeder is used to produce particles with diameters between 1 and 10 μm. The seeding is introduced directly downstream of the airfoil and is allowed to circulate through the tunnel before measurements begin. Velocity field measurements are obtained for angles of attack between 10 and 18 deg in 1 deg increments, with 750 statistically independent PIV samples for each angle.

To be able to simulate real applications with a dynamically varying angle of attack, the setup is designed to allow dynamic pitching of the airfoil with the use of a micro-stepping motor controllable in speed and position. Because the PIV camera's area of focus corresponds to the computational domain used for POD/MLSM calculations, the camera domain is fixed in the airfoil coordinate so that the camera follows the movement of the airfoil at all times. The cameras are mounted on a structure linked to the hinge of the airfoil, to allow the airfoil and cameras to rotate in unison about the same axis. The PIV laser is fixed in space and positioned outside the test section, as shown in Fig. 1.

Concurrently, the unsteady fluctuating pressure is measured at 11 locations along the chord. The 11 unsteady pressure transducers' output signals are sampled simultaneously at a rate of $f_s = 10$ kHz, using a National Instruments SCXI/PXI signal conditioning/data acquisition platform. The PXI analog-to-digital converter board has an internal trigger for simultaneous sampling between channels, ensuring that all the pressure measurements acquired are exactly synchronized. The PIV trigger is also recorded and used to temporally link pressure measurements to the PIV velocity measurements. The phase-aligned information (velocity field and pressure at the surface of the wing) is input to the POD/MLSM algorithms.

D. Flow Separation on the NACA-4412

The need for the whole wing to be in the PIV measurement area for current development of experimental dynamical systems, and the interest in the precise effect of the actuation on the global flow around the airfoil, led us to modify the first PIV setup around the NACA-4412 airfoil model. The previous three-component PIV (3C-PIV) window [11] only covered approximately half of the airfoil's surface and did not show the actuators in the window; therefore, simultaneous 2C-PIV measurements are now performed in two contiguous windows, using wide-angle lenses to increase the measurement area. The two off-axis simultaneous velocity measurements are then dewarped and matched, resulting in one window that contains the whole flow above the airfoil and part of the wake.

Figure 5 shows the flow separation captured by the two-window 2C-PIV measurements as the angle of attack is increased from 10 to 16 deg without applying any control. From $\alpha = 10$ to 15 deg, the trailing-edge boundary-layer separation moves upstream very gradually on the NACA-4412, the wing still has significant lift and small drag in this state, and then leading-edge separation suddenly occurs at $\alpha = 16$ deg. In this study, only the leading-edge separation will be delayed, using the actuators at this position along the chord, but it is believed that the same type of closed-loop control algorithm can be applied to trailing-edge separation control, using actuators located further toward the trailing edge.

The Reynolds number of 135,000 was chosen to approach, as much as possible, the conditions used by Carlson et al. [12] at Clear Science Corporation in their simulations of the flow over a NACA-4412 model. This Reynolds number is also close to typical unmanned air vehicle (UAV) flows. The same type of control would also certainly be appropriate for much higher Reynolds numbers (e.g., civil applications), because the low-dimensional POD approach has proven its effectiveness in even high-speed flows [13], just as well as low-speed flows.

III. Low-Dimensional Analysis

A. Classical Proper Orthogonal Decomposition

In 1967, Lumley [1] proposed the proper orthogonal decomposition as an unbiased technique for studying coherent structures in turbulent flows. The POD is a logical way to build basis functions that capture the most energetic features of the flow [14]. This results in the localization of a small number of structures that contain a large percentage of the system's energy. It must be emphasized that the POD (as described next) is a method that enables an optimal low-dimensional representation of the energy contained in the flow at a given time. This formulation may not be optimal for representing the dynamics of the flow, which could be of interest for closed-loop control. Efforts in modifying the formulation of the POD have been made by Rowley et al. [15] to include the dynamically important information contained in a compressible flow. The POD is a straightforward mathematical approach based on the Karhunen–Loeve expansion. It is used to decompose the velocity field into a finite number of empirical functions intrinsic to the flow, which can be used to ascertain a subspace in which a model can be constructed by projecting the governing equations on it [16]. These eigenfunctions $\phi^{(n)}_{n\in[0,N_{\text{tot}}]}$ are linearly independent and form a basis set chosen to maximize the mean square projection of the velocity field; therefore, POD describes, in an *optimal* way, the energy contained in the flow. This "classical" version of the proper orthogonal decomposition was applied in this study to the fluctuating

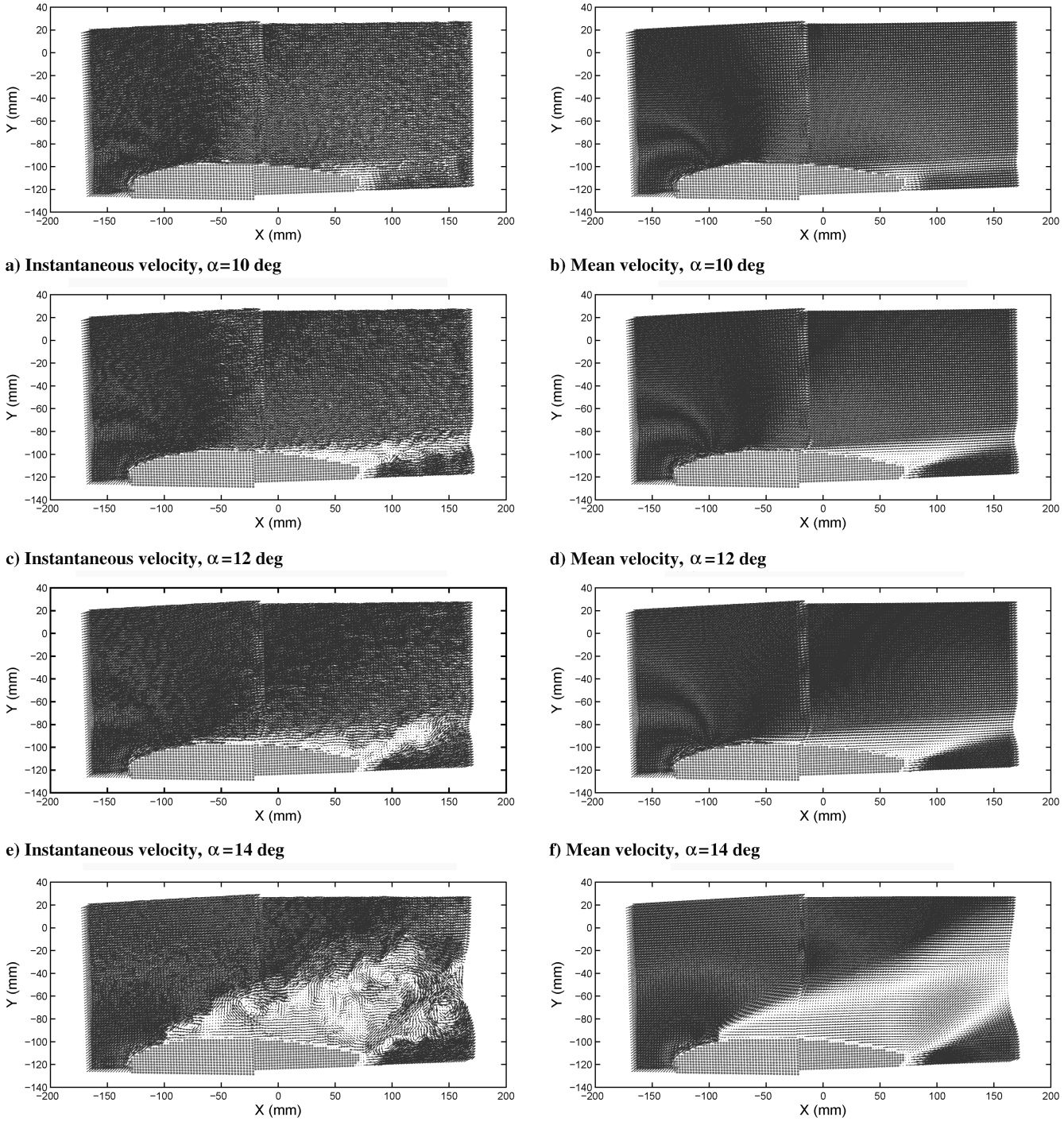

a) Instantaneous velocity, α=10 deg

b) Mean velocity, α=10 deg

c) Instantaneous velocity, α=12 deg

d) Mean velocity, α=12 deg

e) Instantaneous velocity, α=14 deg

f) Mean velocity, α=14 deg

g) Instantaneous velocity, α=16 deg

h) Mean velocity, α=16 deg

Fig. 5 Instantaneous and mean PIV velocity fields for $\alpha = 10$–16 deg.

velocity field by Ausseur and Pinier [7,11], to get a low-dimensional interpretation of the most energetic events present in the incipiently separating region of the airfoil. In that previous setup, the 3C-PIV window had a lower resolution and smaller size to capture only the separating region of the flow. The larger PIV window and higher resolution in the new setup led us to use the snapshot POD (as described in the next paragraph), which is better suited for high spatial resolution data. The POD maximizes the energy content of the flow in an orthonormal basis of functions $\phi^{(n)}(\boldsymbol{x})$, solution of the following integral problem, using the Einstein notation

$$\int_D R_{ij}(\boldsymbol{x}, \boldsymbol{x}')\phi_j^{(n)}(\boldsymbol{x}')\,\mathrm{d}\boldsymbol{x}' = \lambda^{(n)}\phi_i^{(n)}(\boldsymbol{x}) \tag{1}$$

where $R_{ij}(\boldsymbol{x}, \boldsymbol{x}')$ is the ensemble averaged two-point spatial velocity correlation tensor, defined as

$$R_{ij}(\boldsymbol{x}, \boldsymbol{x}') = \langle u_i(\boldsymbol{x}, t_o)u_j(\boldsymbol{x}', t_o)\rangle \tag{2}$$

where t_o is a given PIV-snapshot time and $\langle\cdot\rangle$ denotes average over time. We then can extract the time-dependent (but not time-resolved) expansion coefficients describing the flow, by projecting the PIV velocity field onto the eigenfunctions, as follows:

$$a_n(t_o) = \int_D u_i(\boldsymbol{x}, t_o)\phi_i^{(n)}(\boldsymbol{x})\,\mathrm{d}\boldsymbol{x} \tag{3}$$

where $u_i(\boldsymbol{x}, t_o)$ is the velocity field at a given PIV-snapshot time.

The eigenfunctions $\phi^{(n)}(\boldsymbol{x})$ of Eq. (1) give the optimal basis in terms of energy and are empirical eigenfunctions, because they are derived from the measurement ensemble. The Hilbert–Schmidt theory ensures that if the random field occurs over a finite domain, an infinite number of orthonormal solutions can be used to express the original random velocity field $u_i(\boldsymbol{x}, t_o)$; therefore, we can then partially or totally reconstruct the original velocity field by projecting $a_n(t_o)$ onto the eigenfunctions:

$$u_i(\boldsymbol{x}, t_o) = \sum_{n=1}^{N_m} a_n(t_o)\phi_i^{(n)}(\boldsymbol{x}) \tag{4}$$

where N_m is the number of modes with which we wish to reconstruct the velocity field. If N_m is chosen to be N_{tot}, the velocity field is totally and exactly reconstructed. N_m can be set to a finite number to result in a low-dimensional reconstruction of the flowfield. Using the POD, most of the flow's kinetic energy can be captured in a small number of modes relative to the total number of modes, enabling an accurate representation of the larger coherent structures in terms of energy.

Depending on the data included in the ensemble averages involved in the calculation of the two-point spatial velocity correlation tensor R_{ij}, we will refer to the POD method as either *conditional* or *global*. The conditional approach solves each flow state (angle of attack, Reynolds number, and control on/off) separately; the kernel, therefore, becomes of the following form:

$$R_{ij}(\boldsymbol{x}, \boldsymbol{x}', \alpha) = \langle u_i(\boldsymbol{x}, t_o, \alpha) u_j(\boldsymbol{x}', t_o, \alpha) \rangle \tag{5}$$

whereas the global POD approach includes ensembles of different flow states in the average process, as follows, with $\langle \cdot \rangle_\alpha$ denoting average over α:

$$R_{ij}(\boldsymbol{x}, \boldsymbol{x}') = \langle R_{ij}(\boldsymbol{x}, \boldsymbol{x}', \alpha) \rangle_\alpha \tag{6}$$

Therefore, the eigenfunctions of the global POD have a greater knowledge of the multiple flow states (i.e., for different angles of attack or control on and off). Taylor and Glauser [3] discuss this approach at length. Boree [17] and Fogleman et al. [18] apply a similar approach to an engine cylinder flow. Substituting either the conditional or global kernel into Eq. (1) provides the desired basis functions. The velocity reconstructions displayed in this paper use a global POD approach.

B. Snapshot POD

The wider velocity field provided by the two-window 2C-PIV is important to capture the global effect of the actuation on the flow, near the actuators as well as in the wake. The velocity vector map is now composed of $N = 16637$ vectors with $T = 750$ statistically independent PIV velocity vector maps or snapshots for each case. In cases in which the number of grid points is much greater than the number of snapshots, it is more appropriate and equivalent mathematically to use the snapshots method of the POD, introduced by Sirovich [19] in 1987 to reduce the dimension of the eigenvalue problem. This method reduces the problem to the dimension of T, instead of $n_c \times N$ as with the classical POD method. In this case, the integral eigenvalue problem from Eq. (1) is equivalent to

$$\int_T C(t, t') a_n(t')\, \mathrm{d}t' = \lambda^{(n)} a_n(t) \tag{7}$$

where $C(t, t')$ is now defined as

$$C(t, t') = \frac{1}{T} \int_{\mathcal{D}} u_i(\boldsymbol{x}, t) u_i(\boldsymbol{x}, t')\, \mathrm{d}\boldsymbol{x} \tag{8}$$

and $a_n(t)$ are the temporal eigenfunctions. For reasons of consistency with the classical POD, the latter are arbitrarily chosen to satisfy the following relation:

$$\langle a_m \cdot a_n \rangle = \lambda^{(m)} \delta_{mn} \tag{9}$$

The spatial eigenfunctions $\phi_i^{(n)}(\boldsymbol{x})$ must then be defined as

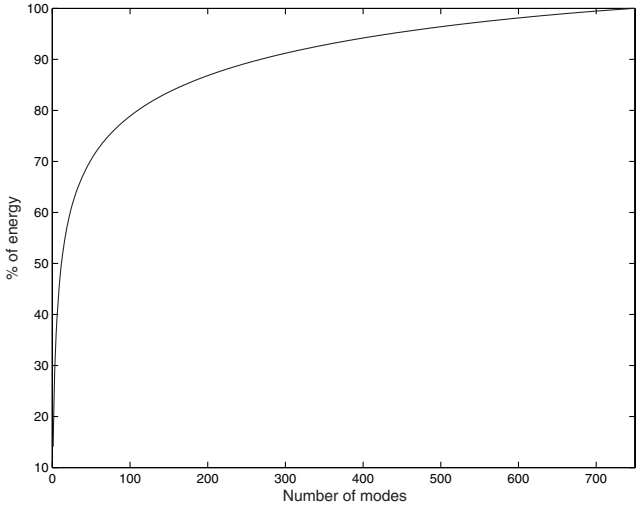

Fig. 6 Cumulative convergence of the energy, using the snapshot POD.

$$\phi_i^{(n)}(\boldsymbol{x}) = \frac{1}{T \cdot \lambda^{(n)}} \int_T a_n(t) u_i(\boldsymbol{x}, t) \tag{10}$$

so that they become orthonormal and verify

$$\int_{\mathcal{D}} \phi_i^{(m)}(\boldsymbol{x}) \phi_i^{(n)}(\boldsymbol{x})\, \mathrm{d}\boldsymbol{x} = \delta_{mn} \tag{11}$$

The low-dimensional velocity fields are then reconstructed by projecting the temporal eigenfunctions $a_n(t)$ onto the spatial eigenfunctions $\phi^{(n)}(\boldsymbol{x})$, using Eq. (4).

As can be seen in Fig. 6, 70% of the energy is retrieved with approximately 7% of the modes. Figure 7 shows a snapshot POD reconstruction of the fluctuating velocity field at the same instant, using 50 out of 750 modes. Using two components of velocity, approximately 15% of the energy is contained in the first mode, which is quite significant in a fully turbulent flow; hence, we proposed [6] to use a simple closed-loop control, using only the first POD mode to be fed back to the actuators. This method was shown to be effective in at least representing the structures with the most energy in the flow [7], but was only a first step toward more sophisticated experimental real-time control of a separating flow.

C. Modified Linear/Quadratic Stochastic Measurements

The linear stochastic estimation (LSE) was proposed by Adrian [20] in 1975. He recognized that the statistical information contained within the two-point correlation tensor R_{ij} could be combined with instantaneous information to form a technique for estimating the flowfield. Cole et al. [21] successfully estimated the radial distribution of the velocity across an axisymmetric jet shear layer, using information from only a few radial locations. Bonnet et al. [2] expanded on the work of Adrian and Cole et al. to form the complementary technique, which combines the POD and LSE to obtain the time-dependent POD expansion coefficients from instantaneous velocity data on coarse hot wire grids. Taylor and Glauser [3] further expanded these methods and demonstrated how instantaneous wall pressure measurements could be used to construct an accurate representation of the instantaneous velocity field from wall pressure alone (i.e., the modified complementary technique or MLSE, now termed MLSM).

To be able to estimate the state of the flow above the NACA-4412 airfoil at all times from wall pressure alone, the MLSM was used by Ausseur and Pinier [11] and Glauser et al. [7]. This technique enables a direct measurement of the low-dimensional expansion coefficient $\tilde{a}_n(t)$ of the flow from a reduced number of sensors located on the wing surface. For each POD mode n, we can describe the estimated POD expansion coefficient as a series expansion, using the discrete instantaneous surface pressure measurements $p_i(t)$ at each streamwise position i on the airfoil surface:

$$\tilde{a}_n(t) = A_{ni}p_i(t) + B_{nij}p_i(t)p_j(t) + C_{nijk}p_i(t)p_j(t)p_k(t) + \ldots \qquad i,j,k \in [1,q] \tag{12}$$

This expansion can then be truncated above the linear term (MLSM) or the quadratic term (MQSM) to estimate the expansion coefficient directly. To minimize the mean square error defined as

$$e_{\tilde{a}_n} = \langle [\tilde{a}_n(t) - a_n(t)]^2 \rangle \tag{13}$$

we solve the following matrix problem of size q for A_{ni} in the linear estimation (MLSM)

$$\begin{bmatrix} \langle p_1p_1\rangle & \cdots & \langle p_qp_1\rangle \\ \vdots & \ddots & \vdots \\ \langle p_1p_q\rangle & \cdots & \langle p_qp_q\rangle \end{bmatrix} \begin{bmatrix} A_{n1} \\ \vdots \\ A_{nq} \end{bmatrix} = \begin{bmatrix} \langle a_np_1\rangle \\ \vdots \\ \langle a_np_q\rangle \end{bmatrix} \tag{14}$$

or solve the following matrix inversion problem for A'_{ni} and B'_{njk} in the quadratic estimation (MQSM)

$$\begin{bmatrix} \langle p_1p_1\rangle & \cdots & \langle p_qp_1\rangle & \langle p_1p_1p_1\rangle & \cdots & \langle p_qp_qp_1\rangle \\ \vdots & \ddots & \vdots & \vdots & \ddots & \vdots \\ \langle p_1p_q\rangle & \cdots & \langle p_qp_q\rangle & \langle p_1p_1p_q\rangle & \cdots & \langle p_qp_qp_q\rangle \\ \langle p_1p_1p_1\rangle & \cdots & \langle p_qp_1p_1\rangle & \langle p_1p_1p_1p_1\rangle & \cdots & \langle p_qp_qp_1p_1\rangle \\ \vdots & & \vdots & \vdots & & \vdots \\ \langle p_1p_jp_k\rangle & \ddots & \langle p_qp_jp_k\rangle & \langle p_1p_1p_jp_k\rangle & \ddots & \langle p_qp_qp_jp_k\rangle \\ \vdots & & \vdots & \vdots & & \vdots \\ \langle p_1p_qp_q\rangle & \cdots & \langle p_qp_qp_q\rangle & \langle p_1p_1p_qp_q\rangle & \cdots & \langle p_qp_qp_qp_q\rangle \end{bmatrix} \times \begin{bmatrix} A'_{n1} \\ \vdots \\ A'_{nq} \\ B'_{n11} \\ \vdots \\ B'_{njk} \\ \vdots \\ B'_{nqq} \end{bmatrix} = \begin{bmatrix} \langle a_np_1\rangle \\ \vdots \\ \langle a_np_q\rangle \\ \langle a_np_1p_1\rangle \\ \vdots \\ \langle a_np_jp_k\rangle \\ \vdots \\ \langle a_np_qp_q\rangle \end{bmatrix} \tag{15}$$

Note that $\langle p_jp_k\rangle$ and $\langle p_kp_j\rangle$ are identical. Therefore, to prevent redundancy in the formulation, only the terms where $k \geq j$ are computed in this problem. Hence, the size of the problem is $q + [q(q+1)]/2$ instead of $q + q^2$. Given A_{ni}, or A'_{ni} and B'_{njk}, the estimated expansion coefficient is then estimated in real-time, using the following simple matrix multiplications:

$$\text{MLSM}: \tilde{a}_n(t) = A_{ni}p_i(t) \tag{16}$$

$$\text{MQSM}: \tilde{a}_n(t) = A'_{ni}p_i(t) + B'_{njk}p_j(t)p_k(t) \tag{17}$$

When using the wall pressure to estimate the boundary-layer flowfield, both linear and quadratic terms should be kept to be able to accurately estimate the conditional event [22]. Murray and Ukeiley [23] also showed that the quadratic estimation procedure was far more effective than the linear estimation when sensing surface pressure to estimate the flowfield in a cavity. Here, we present experimental results comparing reconstructions with the linear (MLSM) and quadratic (MQSM) techniques, directly estimating the expansion coefficient $a_n(t)$ instead of estimating the velocity (LSE). It can be shown that the LSE/QSE and the MLSM/MQSM procedures are exactly equivalent, but the latter are much faster computationally, because many of the velocity correlations are already contained in the previously computed expansion coefficient. Therefore, the MLSM/MQSM will be preferred for its suitability to real-time computations at high loop rates. Figure 8 shows the linear (using MLSM) and quadratic (using MQSM) reconstructions of the fluctuating velocity field. It is clear that the addition of the quadratic term enables a much better representation of the flowfield and we are able to retrieve a greater part of the energy contained in the flow.

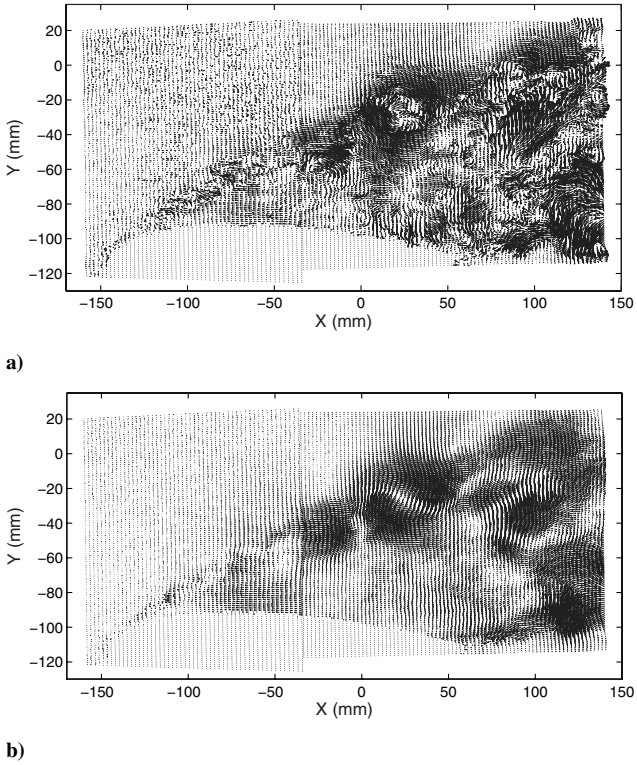

Fig. 7 Comparison of a) the original fluctuating velocity field and b) the snapshot POD reconstruction using 50 modes at $\alpha = 17.5$ deg, $t = 550$, and control off.

IV. Proportional Closed-Loop Feedback Control

When implementing control in practical situations, it is important to make sure the control method is overall cost-efficient; therefore, we use a minimal actuation input with an order one incidence on the flow. Advantages in energy cost of using closed-loop instead of open-loop control are discussed further in this section. In particular, our aim is to keep the feedback control always active and the flow at all times attached, because we show that a lot more energy is required to reattach a separated flow than to keep a flow attached. Furthermore, in a practical situation, the separated flow case is usually undesirable.

As shown by Glauser et al. [6], the MLSM method provides a reasonable estimate of the velocity field above the airfoil. We use the POD coefficients obtained from Eq. (16) as a time series to drive the actuators via a simple proportional feedback loop. Figure 9 shows the time series for the first four estimated POD/MLSM coefficients at the incipiently separating condition ($\alpha = 15$ deg). As can be seen from these time series, global POD mode 1 has the largest amplitude and lowest frequencies. Therefore, using this mode as an output of the actuators should have the biggest impact on the flow. We want to minimize the error between the estimated time-dependent POD coefficient $\tilde{a}_1(t)$ and the desired state in which the flow is fully attached and the fluctuations of the POD/MLSM coefficient are thus 0. This can be written as $\epsilon(t) = \tilde{a}_1(t)$. The actuators are, therefore, driven by

$$\text{Act}_{\text{input}} = A \cdot \epsilon(t) \sin(2\pi f_o t) \tag{18}$$

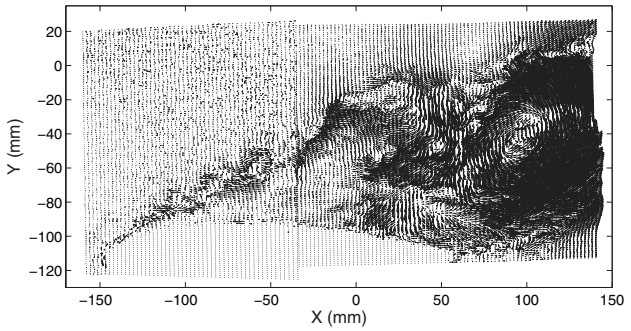

a) Original fluctuating

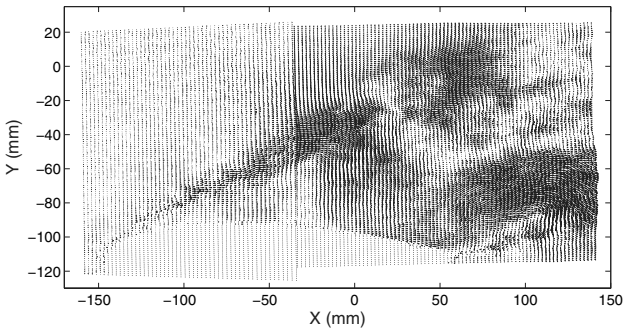

b) Linear estimate from MLSM

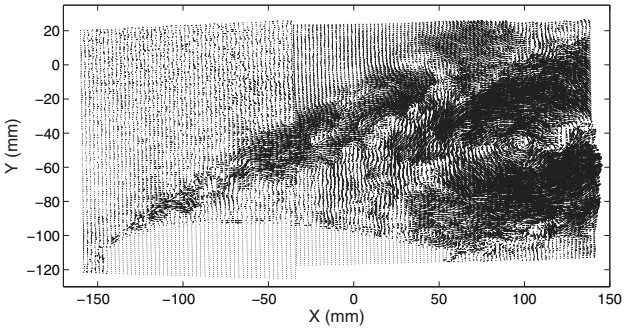

c) Quadratic estimate from MQSM

Fig. 8 Comparison of linear and quadratic estimates of the fluctuating velocity field at $\alpha = 17.5$ deg, $t = 567$, and control off.

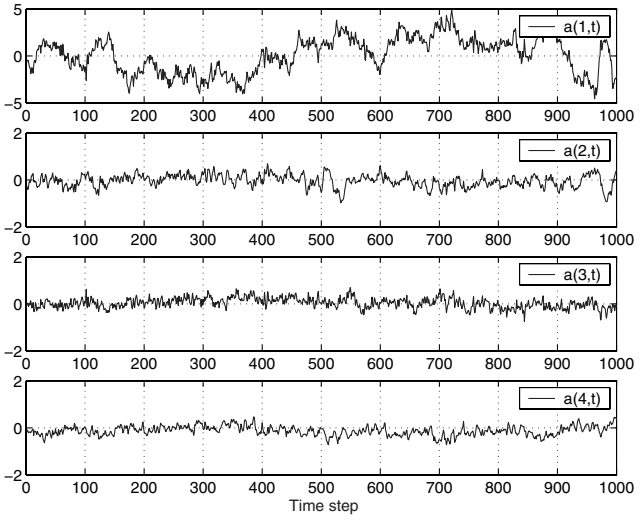

Fig. 9 Time-resolved estimates of first four global POD coefficients from airfoil surface pressure measurements at $\alpha = 15$ deg.

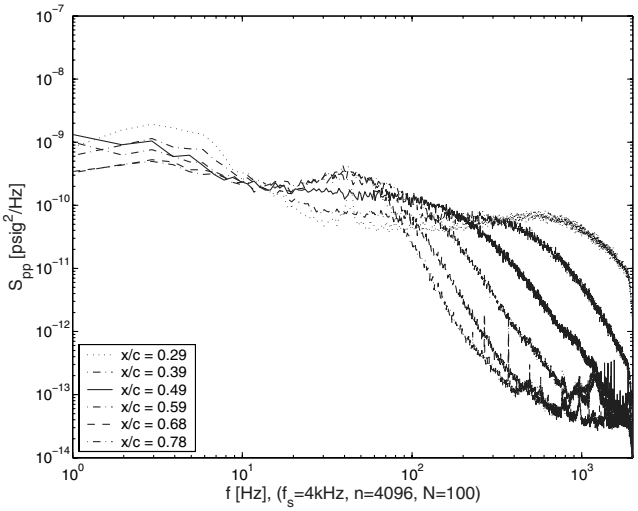

Fig. 10 Airfoil surface pressure spectra at $\alpha = 15$ deg and control off.

where gain A is selected based on open-loop results. In this form, we are using the time series from the POD/MLSM coefficient $\tilde{a}_1(t)$ to modulate the amplitude of the carrier sine wave of frequency $f_o = 800$ Hz, the resonance frequency of the cavity/actuator system. Typical flow separation events occur at a much lower bandwidth ($\sim$50 Hz) as can be seen in the surface pressure spectrum shown in Fig. 10. The spectrum of the first POD/MLSM coefficient estimated from the pressure (Fig. 11) shows that it captures the low-frequency vortex shedding at around 50 Hz (or $f^+ \sim 1$). Hence, the amplitude modulation should provide the desirable flow excitation frequency for the current experiment. The acquired data is digitally low-pass filtered at 200 Hz before being fed back to prevent divergence of the actuation amplitude. Indeed, because the actuator signal is fed back to the pressure through the flow, it needs to be filtered out of the pressure signal before computing from it the new actuation output. The errors in the measurement (like the one coming from sensing the actuator signal in the pressure measurement) can be corrected using more advanced filters like Kalman filters, which is the subject of future work. Figure 12 shows the architecture of the proportional feedback control actuation loop. The effect of the closed-loop control can be seen in Fig. 13, showing the mean velocity fields at $\alpha = 16$ deg, control on and off, with a clear delay of the leading-edge separation when the control is active.

Figure 14a shows the first POD coefficient estimated from surface pressure only (without actuation), low-pass filtered at 200 Hz, modulating the 800-Hz wave (which we eventually use to drive the actuators) from $\alpha = 12$ to 16 deg.

Here are the key points from this figure:

1) The rms amplitude of the estimated POD coefficient $\tilde{a}_1(t)$ increases with the angle of attack, as it senses the incipient separation and the growing structures in the boundary layer. This is a *necessary condition* for the method to be stable and autonomous. Figure 15 shows how this condition leads to a stable limit cycle. Without this condition satisfied, the actuation amplitude would either diverge or it would go to zero and the flow would separate. It is important to note that this is obtained from surface pressure, a practical variable to measure, processed through the POD/MLSM algorithm.

2) The separated flow at $\alpha = 16$ deg reveals a significantly larger rms amplitude than that at the lower angles of attack, capturing the onset of separation, although no cases of separated flow were included in the POD eigenfunctions. Even when the flow separates, the control output grows larger and is able to reattach the flow. This demonstrates the relative robustness of the method, still stable out of the prescribed range of application.

3) The modulation signal estimated from the POD/MLSM method shows low-frequency information better tuned with the boundary-layer time scales [in particular, the band from 50 to 100 Hz ($f^+ \sim 1$)], as seen in Fig. 11. Hence, from the estimated POD coefficient, we are getting the relevant amplitude and frequency information for driving

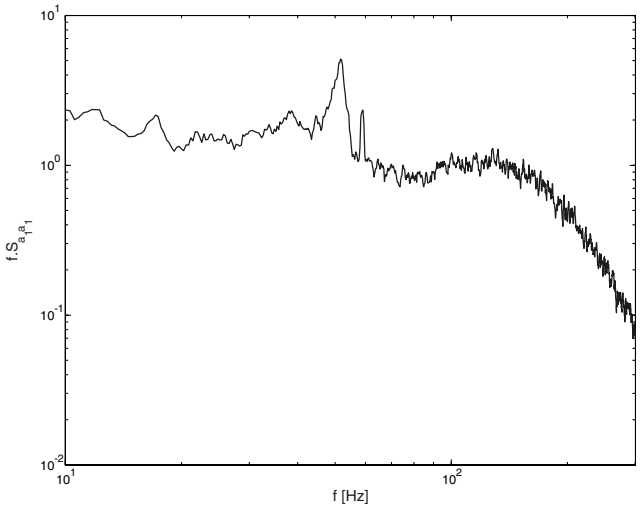

Fig. 11 Estimated POD/MLSM coefficient spectrum at $\alpha = 14$ deg, mode 1, and control off.

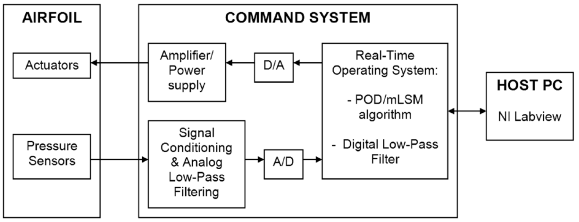

Fig. 12 Proportional closed-loop control architecture.

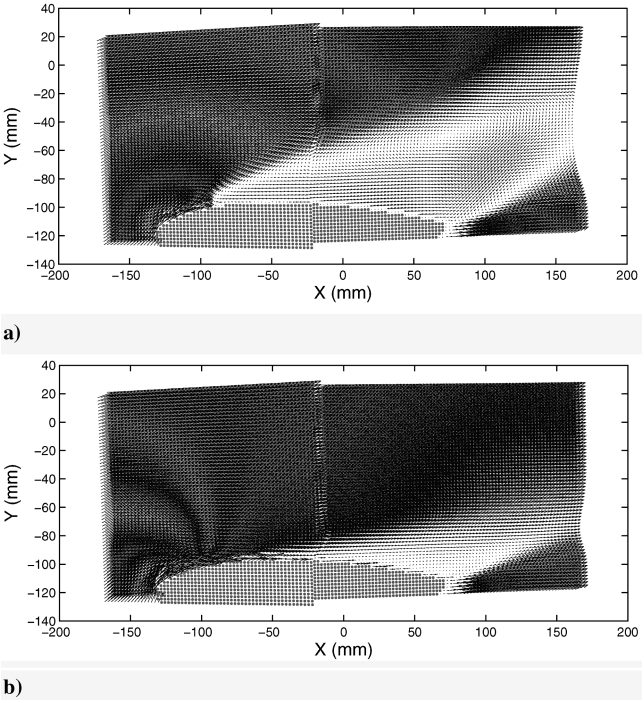

Fig. 13 Mean velocity field at $\alpha = 16$ deg: a) control off and b) control on.

the actuators in a feedback flow control loop. Next, we show how this is used in a real-time proportional feedback control loop.

Figure 14b shows the first POD coefficient estimated from wall pressure, low-pass filtered at 200 Hz for stability reasons, amplitude modulating the 800 Hz wave, which is fed back to the actuators, using Eq. (18). At $\alpha = 12$, 13, and 14 deg, the actuation has little effect on the flow, as seen in Fig. 14b. This is because the control is properly tracking the amplitude and, because the flow is attached, the structures are small and the amplitude is low. At $\alpha = 15$ deg, the actuation does decrease the amplitude of the coefficients, a necessary criterion for the control to be stable. We are able to delay separation beyond $\alpha = 18$ deg (notice the rms amplitude is still lower than that of $\alpha = 16$ deg, separated as shown in Fig. 14a) without optimizing the actuation and with a rather low rms output from the actuators.

Figure 16 shows the signature of the transient unsteady separation of the flow as we stop the actuators. Note the transition region in which the actuation is off and the flow is starting to separate. This is a hysteresis phenomenon of duration on the order of 1 s, which has also been observed by Wygnanski [24] on real-scale applications of open-loop actuation. We plot both the actuator signal (the POD coefficient low-pass filtered at 200 Hz, modulating the 800 Hz sine wave) and the unfiltered POD coefficient itself. The coefficients grow in amplitude when the flow separates and they also change in frequency content from higher (attached turbulent boundary layer) to lower frequencies as the signature of the large eddies associated with the unsteady incipient separation is sensed. These results clearly show that the estimated first POD mode coefficient (via the POD/MLSM method) contains the necessary low-dimensional signature for performing practical feedback flow control.

The benefits of closed-loop feedback control compared with open-loop control appear to be significant. Even though it is not shown that closed-loop control performs better than open-loop control in a static case (or fixed angle of attack), it is clear that closed-loop control constitutes a more autonomous and energy efficient system. Figure 17 shows the rms actuation (before amplification) needed to keep the flow attached during a pitching maneuver from $\alpha = 12$ deg to $\alpha = 17$ deg at a constant pitching rate. The amplitude of the open-loop control is constant and fixed at the amplitude required to keep the flow attached at $\alpha = 17$ deg. The closed-loop control is turned on at $\alpha = 12$ deg and autonomously adjusts its amplitude according to the real-time estimate of the flowfield state throughout the pitching maneuver. The cost reduction brought by using a simple closed-loop system is represented by the shaded area between both curves. In arbitrary units, by integrating each curve, a power requirement can be computed to quantify the savings: this computation yields a 34% energy savings brought by using closed-loop control in this particular maneuver. The curve corresponding to the required actuation at fixed angles of attack means the control is turned on only once the airfoil is set at each angle. It is seen that it takes much more energy to reattach the flow once it has separated (e.g., at $\alpha = 16$ deg) than to maintain attached flow all along. This test demonstrates two points:

1) It is critical to keep the control active and the flow attached at all times to achieve the control objective without excessive power need.

2) Closed-loop control offers significant savings in terms of power consumption over open-loop control during dynamical maneuvers or unsteady flows.

The advantage of closed-loop control, therefore, lies in the fact that the control output adjusts autonomously according to the state of the flow, whereas open-loop control will require a priori knowledge of the maximum output that will be needed and the output will have to remain at the maximum level all along, even when not needed. For cases in which a vehicle is subjected to unpredictable flow dynamics like unsteady gusts of wind or sharp maneuvers, closed-loop flow control is certainly more appropriate. One can also optimize the control loop using modern control algorithms to further reduce the energy consumption and improve the overall efficiency of the flow control. Before implementation on a practical system, a more in-depth study would have to be led in order to quantify and compare the performance of open-loop and closed-loop control in terms of lift and drag, quantities that were not measured in the present study. Furthermore, work is in progress toward the development of an experimental reduced-order model that explicitly includes the actuation input [25] for optimizing the efficiency and robustness of the feedback flow control. Such work has been successful in controlling subsonic cavity flows [26] and shows great promise in the development of such models for flow separation control.

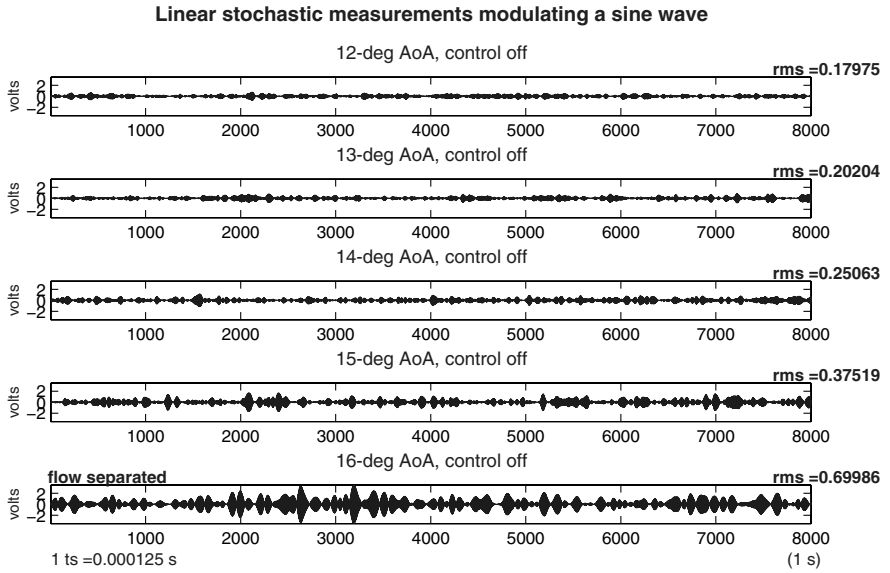

a) Control OFF, α =12–16°

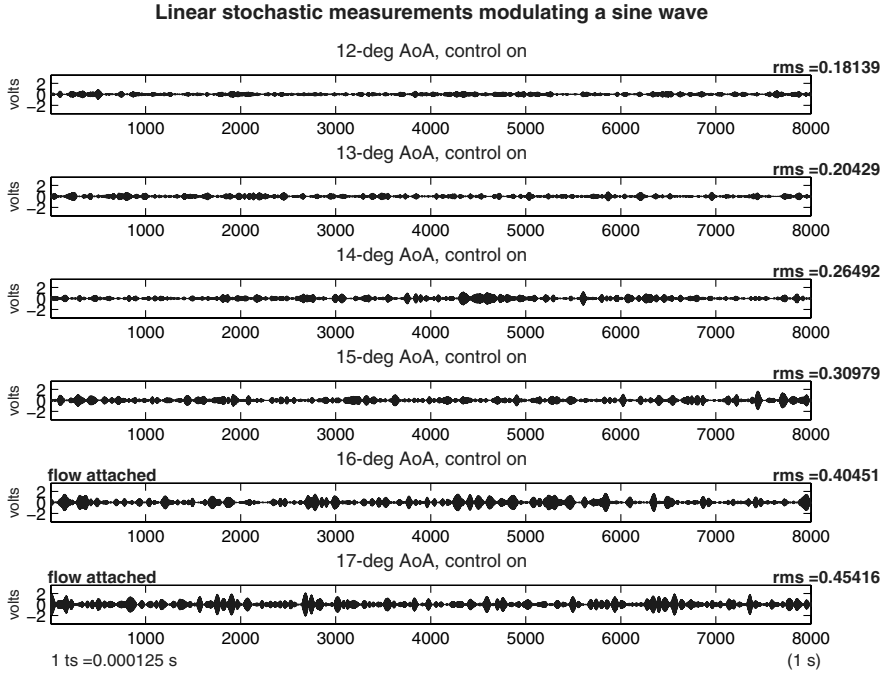

b) Control ON, $\alpha = 12 - 17°$

Fig. 14 First POD coefficient estimated from wall pressure modulating 800-Hz sine wave.

V. Conclusions

The estimated first POD coefficient provides the relevant amplitude and frequency information for driving the actuators in an autonomous feedback flow control loop. We also demonstrate the success of using these time-dependent coefficients, estimated from

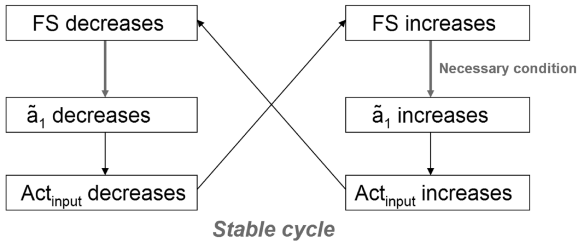

Fig. 15 Stability cycle for the closed-loop control (FS indicates flow separation).

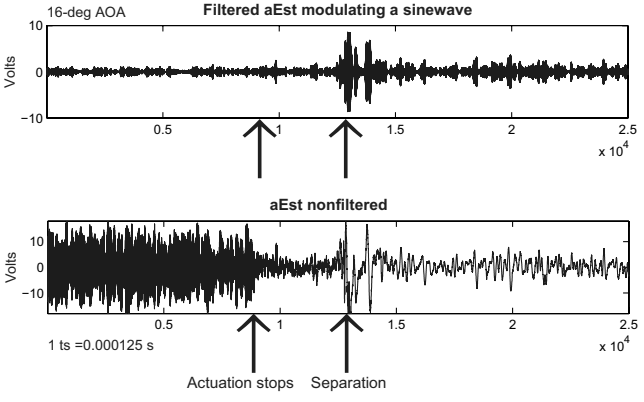

Fig. 16 Coefficients with feedback control on and then off.

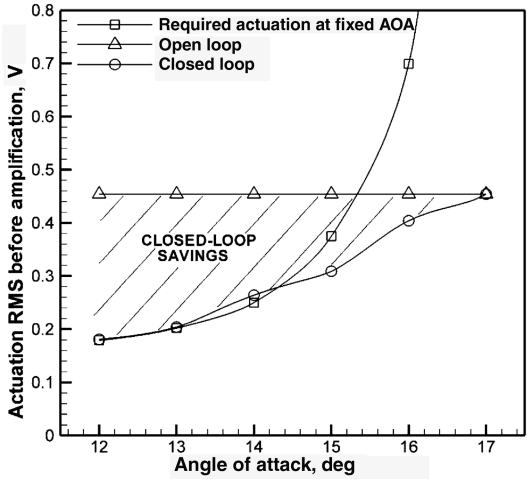

Fig. 17 Closed-loop control benefits.

surface pressure only, for use in an applicable simple proportional feedback loop to delay flow separation. What is particularly promising is that this technique showed to be successful in a flow that is turbulent and incipiently separating. There is, furthermore, much assurance that these kinds of low-dimensional techniques would be efficient at much higher Reynolds numbers. We also find, in a control on/off scenario, that the estimated first POD mode coefficient contains the necessary low-dimensional signature of the unsteady incipiently separating flow phenomena for performing practical feedback flow control. These results are very encouraging in that they show that proportional feedback control is feasible from an estimated measurement of the first POD coefficient. This methodology is critical for implementation of realistic feedback flow control, because inflow measurements are impractical and surface measurements are required in most applications. The results presented here validate the use of low-dimensional plant estimates for developing more sophisticated controller designs as a promising solution for real-time flow separation control.

Acknowledgments

The authors gratefully acknowledge the support of the U.S. Air Force Office of Scientific Research through a Phase 2 Small Business Technology Transfer (STTR) with Clear Science Corporation and the New York State Office of Science, Technology and Academic Research (STAR) via the STAR Center in Environmental Quality Systems and the Syracuse University CASE Center. The authors would like to thank Henry Carlson of Clear Science Corp. for many interactions, in particular, those leading to the content of Fig. 17.

References

[1] Lumley, J. L., "The Structure of Inhomogeneous Turbulent Flows," *Atmospheric Turbulence and Radio Wave Propagation*, edited by A. M. Yaglom and V. I. Tatarsky, Nauka, Moscow, 1967, pp. 166–178.

[2] Bonnet, J. P., Cole, D. R., Delville, J., Glauser, M. N., and Ukeiley, L. S., "Stochastic Estimation and Proper Orthogonal Decomposition: Complementary Techniques for Identifying Structure," *Experiments in Fluids*, Vol. 17, No. 5, 1994, pp. 307–314.

[3] Taylor, J. A., and Glauser, M. N., "Toward Practical Flow Sensing and Control Via POD and LSE Based Low-Dimensional Tools," *Journal of Fluids Engineering*, Vol. 126, No. 3, 2004, pp. 337–345; also American Society of Mechanical Engineers Paper FEDSM2002-31416, 2002.

[4] Cohen, K., Siegel, S., McLaughlin, T., and Gillies, E., "Feedback Control of a Cylinder Wake Low-Dimensional Model," *AIAA Journal*, Vol. 41, No. 7, 2003, pp. 1389–91.

[5] Schmit, R. F., and Glauser, M. N., "Use of Low-Dimensional Methods for Wake Flowfield Estimation from Dynamic Strain," *AIAA Journal*, Vol. 43, No. 5, 2005, pp. 1133–1136.

[6] Glauser, M., Young, M., Higuchi, H., Tinney, C., and Carlson, H., "POD Based Experimental Flow Control on a NACA-4412 Airfoil," AIAA Paper 2004-0575, 2004.

[7] Glauser, M. N., Higuchi, H., Ausseur, J. M., and Pinier, J. T., "Feedback Control of Separated Flows," AIAA Paper 2004-2521, 2004.

[8] Smith, B., and Glezer, A., "The Formation and Evolution of Synthetic Jets," *Physics of Fluids*, Vol. 10, No. 9, 1998, pp. 2281–2297.

[9] Glezer, A., and Amitay, M., "Synthetic Jets," *Annual Review of Fluid Mechanics*, Vol. 34, 2002, pp. 503–529.

[10] Margalit, S., Greenblatt, D., Seifert, A., and Wygnanski, I., "Delta Wing Stall and Roll Control Using Segmented Piezoelectric Fluidic Actuators," *Journal of Aircraft*, Vol. 42, No. 3, 2005, pp. 698–709.

[11] Ausseur, J., and Pinier, J., "Toward Closed-Loop Feedback Control of the Flow Over NACA-4412 Airfoil," AIAA Paper 2005-0343, 2005.

[12] Carlson, H., Roveda, R., Glauser, M., "Models for Controlling Airfoil Lift and Drag," AIAA Paper 2004-0579, 2004.

[13] Tinney, C. E., Ukeiley, L., and Glauser, M. N., "Noise Identification in a Mach 0.85 Jet Using Modified Low-Dimensional Techniques," *Proceedings of the Tenth European Turbulence Conference*, edited by Anderson, H. I., and Krogstad, P. A., Vol. 168, International Center for Numerical Methods in Engineering (CIMNE), Barcelona, 2004, pp. 1–4.

[14] Holmes, P. J., Lumley, J. L., Berkooz, G., Mattingly, J. C., and Wittenberg, R. W., "Low-Dimensional Models of Coherent Structures in Turbulence," *Physics Reports*, Vol. 287, No. 4, 1997, pp. 337–384.

[15] Rowley, C., Colonius, T., Murray, R., "Model Reduction for Compressible Flows Using POD and Galerkin Projection," *Physica D*, Vol. 189, Nos. 1–2, Feb. 2004, pp. 115–129.

[16] Holmes, P. J., Lumley, J. L., and Berkooz, G., *Turbulence, Coherent Structures, Dynamical Systems and Symmetry*, Cambridge Univ. Press, Cambridge, England, U.K., 1996.

[17] Boree, J., "Extended Proper Othogonal Decomposition: A Tool to Analyse Correlated Events in Turbulent Flows," *Experiments in Fluids*, Vol. 35, No. 2, 2003, pp. 188–192.

[18] Fogleman, M., Lumley, J., Rempfer, D., and Haworth, D., "Application of the Proper Orthogonal Decomposition to Datasets of Internal Combustion Engine Flows," *Journal of Turbulence*, Vol. 5, No. 23, 2004, pp. 1–18.

[19] Sirovich, L., "Turbulence and the Dynamics of Coherent Structures," Parts 1, 2, and 3, *Quarterly of Applied Mathematics*, Vol. 45, No. 3, 1987, pp. 561–590.

[20] Adrian, R. J., "On the Role of Conditional Averages in Turbulence Theory," *Turbulence in Liquids: Proceedings of the Fourth Biennial Symposium on Turbulence in Liquids*, edited by Zakin, J., and Patterson, G., Science Press, New South Wales, Australia, 1977, pp. 323–332.

[21] Cole, D. R., Glauser, M. N., and Guezennec, Y. G., "An Application of Stochastic Estimation to the Jet Mixing Layer," *Physics of Fluids*, Vol. 4, No. 1, 1991, pp. 192–194.

[22] Naguib, A., Wark, C., and Juckenhoefel, O., "Stochastic Estimation and Flow Sources Associated with Surface Pressure Events in a Turbulent Boundary Layer," *Physics of Fluids*, Vol. 13, No. 9, 2001, pp. 2611–2616.

[23] Murray, N., and Ukeiley, L., "Estimating the Shear Layer Velocity Field Above an Open Cavity from Surface Pressure Measurements," AIAA Paper 2002-2866, 2002.

[24] Wygnanski, I., "The Variables Affecting the Control of Separation by Periodic Excitation," AIAA Paper 2004-2511, 2004.

[25] Ausseur, J., Pinier, J., Glauser, M., Higuchi, H. & Carlson, H., "Controller Development for Closed-Loop Feedback Control of Flows," AIAA Paper 2005-5264, 2005.

[26] Debiasi, M., Little, J., Malone, J., Samimy, M., Yan, P., and Özbay, H., "An Experimental Study of Subsonic Cavity Flow: Physical Understanding and Control," AIAA Paper 2004-2123, 2004.

N. Clemens
Associate Editor